




## Article

# Ermeloite, $\text{AlPO}_4 \cdot \text{H}_2\text{O}$ a new phosphate mineral with kieserite-type structure from Galicia, Spain

Guillermo Z. Vérez<sup>1</sup> , Carlos J. Rodríguez Vázquez<sup>1</sup>, Bruno Dacuña Mariño<sup>1</sup>, Inés Fernández Cereijo<sup>1</sup>, José González del Tánago<sup>2</sup>, Ramón Jiménez Martínez<sup>3</sup>, Ramiro Barreiro Pérez<sup>1</sup>, Raquel Antón Segurado<sup>1</sup>, Ezequiel Vázquez Fernández<sup>1</sup>, Montse Gómez Dopazo<sup>1</sup>, Aida González Pazos<sup>1</sup> and Oscar Lantes-Suárez<sup>1</sup>

<sup>1</sup>Área de Infraestructuras de Investigación, Universidade de Santiago de Compostela. 15782 Galicia, Spain; <sup>2</sup>Departamento de Mineralogía y Petrología, Facultad de Ciencias Geológicas, Universidad Complutense, 28040 Madrid, Spain; and <sup>3</sup>Departamento de Recursos Geológicos para la Transición Ecológica, Instituto Geológico y Minero de España (CSIC), 28003 Madrid, Spain.

### Abstract

Ermeloite is a new aluminium phosphate mineral from Galicia, Spain, in the northwest of the Iberian Peninsula. It is the third formally recognised mineral discovered in Galicia since morenosite and cervantite in the 19<sup>th</sup> Century. The name and symbol (Erm) were approved by the Commission on New Minerals, Nomenclature and Classification of the International Mineralogical Association (IMA2021–017a) in recognition of the geographical location where it was found. The mineral occurs as a light blue to white fine aggregate over quartz and microcline associated with wardite. Crystals of ~0.04 mm are transparent and have a waxy lustre. The simplified empirical formula determined using electron microprobe analysis is  $\text{Al}_{1.02}\text{P}_{0.95}\text{F}_{0.06}\text{O}_{3.88} \cdot 1.06 \text{H}_2\text{O}$ , which is near to the ideal formula  $\text{Al}(\text{PO}_4) \cdot \text{H}_2\text{O}$ . The mineral is an alteration product within a phosphate pegmatite. Ermeloite is the second phosphate isostructural with the sulfates of the kieserite group. Single-crystal X-ray diffraction showed that ermeloite crystallises in the monoclinic  $C2/c$  space group with cell parameters  $a = 6.5371(4) \text{ \AA}$ ,  $b = 7.5670(5) \text{ \AA}$ ,  $c = 7.1146(5) \text{ \AA}$ ,  $\beta = 115.335(2)^\circ$ ,  $V = 318.08(4) \text{ \AA}^3$  and  $Z = 4$  at room temperature. Comparative analysis of the crystallographic data, with isostructural phosphates, revealed an interesting behaviour for these compounds.

**Keywords:** ermeloite; aluminium phosphate; new mineral; crystal structure; X-ray diffraction; Raman spectroscopy; electron microprobe analysis; pegmatite paragenesis

(Received 2 November 2023; accepted 16 April 2024; Accepted Manuscript published online: 25 April 2024; Associate Editor: Michael Rumsey)

### Introduction

At present, only two minerals whose type locality is in Galicia, Spain are recognised by the International Mineralogical Association (IMA) as unquestionable minerals. These minerals are morenosite from Cabo Ortegal, A Coruña (Martínez Alcibar, 1850, 1851) and cervantite from Cervantes, Lugo (Dufrenoy, 1845). Therefore, ermeloite (Erm) is of great historical and social relevance as it is the first well-characterised mineral discovered in Galicia for more than 150 years. Furthermore, our understanding of the isostructural kieserite group is enhanced by the discovery of ermeloite.

The new mineral was found in a pegmatite outcrop in granodiorites of the Morrazo peninsula (Moaña, Pontevedra, Galicia, Spain). It was found in the southern part of a place known as ‘As Chans de Ermelo’ (42°17’47”N, 8°45’12”W, ETRS89). The

mineral and the name ermeloite have been approved by the Commission on New Minerals, Nomenclature and Classification (CNMNC) of the IMA (IMA2021–017a, Zaragoza Vérez *et al.*, 2022). The type specimen (CMG4083) is kept in the Museo de Historia Natural of the University of Santiago de Compostela as part of the Galician Mineral Collection. The test sample used in the electron microprobe analyses (EMPA) (N° 21610) is kept in the Museo Geominero (CN IGME-CSIC, Madrid, Spain).

### Experimental methods

Wavelength-dispersive EMPA for ermeloite were obtained using a Jeol JXA-8900 instrument at the Universidad Complutense, Madrid, Spain. Standard operating conditions were: accelerating voltage 15 kV, intensity probe current 20 nA, peak counting time 10 s, background counting time 5 s and beam diameter 5  $\mu\text{m}$ . The standards used were almandine ( $\text{FeK}\alpha$ ), microcline ( $\text{KK}\alpha$ ), fluorapatite ( $\text{PK}\alpha$ ,  $\text{FK}\alpha$ ) (Jarosevich *et al.*, 1980) and albite ( $\text{AlK}\alpha$ ) (McGuire *et al.*, 1992). The results were processed with an on-line ZAF programme. The elemental analyses expressed as element wt.% are presented in Supplementary Table S1.

**Corresponding author:** Guillermo Z. Vérez; Email: [g.zaragoza@usc.es](mailto:g.zaragoza@usc.es)

**Cite this article:** Vérez G.Z., Vázquez C.J.R., Mariño B.D., Cereijo I.F., del Tánago J.G., Martínez R.J., Pérez R.B., Segurado R.A., Fernández E.V., Dopazo M.G., Pazos A.G. and Lantes-Suárez O. (2024) Ermeloite,  $\text{AlPO}_4 \cdot \text{H}_2\text{O}$  a new phosphate mineral with kieserite-type structure from Galicia, Spain. *Mineralogical Magazine* 1–9. <https://doi.org/10.1180/mgm.2024.33>

© The Author(s), 2024. Published by Cambridge University Press on behalf of The Mineralogical Society of the United Kingdom and Ireland. This is an Open Access article, distributed under the terms of the Creative Commons Attribution licence (<http://creativecommons.org/licenses/by/4.0/>), which permits unrestricted re-use, distribution and reproduction, provided the original article is properly cited.

The presence of lithium was excluded by optical inductively coupled plasma (ICP) using a PerkinElmer Optima 4300 DV ICP-OES spectrometer equipped with PerkinElmer AS-93plus autosampler. The sample was digested with HCl, HF and HNO<sub>3</sub> in a microwave reactor, for 45 minutes at 250°C.

The Raman spectrum of ermelioite was collected on a randomly oriented crystal using a WITec alpha300 R confocal Raman microscope operated with an ultra-high throughput spectrometer (UHTS300), coupled by fibre to a 532 nm, 6.8 mW solid-state laser and a charge-coupled device (CCD) back-illuminated detector operating at -60°C. A Zeiss EC Epiplan Neofluar 50x/0.8 objective was used. Automatic autofocus and a monochromator grating of 600 grooves/mm were used.

Powder X-ray diffraction (XRD) data were obtained using a Philips PW1710 powder diffractometer with a Philips PW1820/00 vertical goniometer and a FR590 Enraf Nonius X-ray generator. The instrument was equipped with a graphite-diffracted beam monochromator and copper radiation source ( $\lambda$  (CuK $\alpha_1$ ) = 1.5406 Å), operating at 40 kV and 30 mA. Diffraction data were collected using a scintillation counter for a range of 2–65° in 2 $\theta$  with a step size of 0.02° and counting time of 1 s/step. The powdered sample was spread over a low-background plate sample holder (Si 511) to minimise the background noise and the effect of preferred orientation. The sample was spun during the data collection to improve the measurement statistics.

Unit cell parameters indexed by single-crystal XRD were refined using experimental data from a polycrystalline sample by the Pawley method using the *HighScorePlus* software [v. 3.0d (3.0.04), © PANalytical B. V.; Degen *et al.*, 2014]. Peak assignments and intensities for the observed and calculated patterns are shown in Table 1, and a graphical interpretation in Supplementary Fig. S1.

**Table 1.** Powder X-ray diffraction data ( $d$  in Å) for ermelioite. (8 strongest lines in bold). Calculated unit cell parameters: monoclinic C2/c with  $a = 6.5393(32)$ ,  $b = 7.5716(32)$ ,  $c = 7.1200(34)$  Å,  $\beta = 115.337(1)^\circ$ .  $R_p = 8.91$ ,  $R_{wp} = 11.57$ ,  $R_{exp} = 10.97$  and  $GoF = 1.05$ .

$l_{obs}$	$l_{calc}$	$d_{meas}$	$d_{calc}$	$h\ k\ l$
<b>76.56</b>	<b>67.68</b>	<b>4.6611</b>	<b>4.6588</b>	<b>1 1 0</b>
<b>40.54</b>	<b>44.15</b>	<b>4.5800</b>	<b>4.5779</b>	<b>1 1 1</b>
<b>100.00</b>	<b>100.00</b>	<b>3.2850</b>	<b>3.2839</b>	<b>1 1 1</b>
<b>80.02</b>	<b>74.45</b>	<b>3.2640</b>	<b>3.2629</b>	<b>0 2 1</b>
<b>49.44</b>	<b>53.51</b>	<b>3.2010</b>	<b>3.1999</b>	<b>1 1 2</b>
15.88	18.10	2.9560	2.9551	2 0 0
<b>34.79</b>	<b>34.90</b>	<b>2.8745</b>	<b>2.8737</b>	<b>2 0 2</b>
<b>39.55</b>	<b>38.64</b>	<b>2.4742</b>	<b>2.4736</b>	<b>2 2 1</b>
<b>33.42</b>	<b>34.62</b>	<b>2.4522</b>	<b>2.4516</b>	<b>0 2 2</b>
14.96	14.36	2.3088	2.3083	1 1 2
11.55	11.21	2.2894	2.2889	2 2 2
11.29	12.79	2.0753	2.0749	1 3 1
19.48	18.71	2.0560	2.0555	3 1 2
19.14	19.98	2.0536	2.0532	1 3 2
25.79	24.48	1.9867	1.9863	2 2 1
9.52	10.09	1.8666	1.8662	0 2 3
14.65	12.10	1.8576	1.8573	3 1 3
12.36	10.84	1.8226	1.8223	2 0 2
11.55	10.10	1.7386	1.7383	1 1 3
9.05	9.70	1.6414	1.6411	3 3 1
13.48	12.46	1.6317	1.6315	0 4 2
15.26	14.85	1.6002	1.6000	2 2 4
19.14	16.44	1.5986	1.5983	3 1 4
17.80	17.73	1.5941	1.5939	2 4 0
14.65	14.32	1.5262	1.5259	3 3 3
13.48	12.18	1.4581	1.4579	1 3 3

A light-blue crystal suitable for single-crystal XRD (0.05 × 0.04 × 0.03 mm) was carefully selected, using cross-polarised light on an optical microscope with 90× magnification. The measurements were carried out at ambient temperature.

Single-crystal XRD studies were performed on a Bruker D8 Venture Photon III-14 diffractometer using Incoatec multilayer mirror monochromated MoK $\alpha$  radiation ( $\lambda = 0.71073$  Å) from a microfocus sealed tube source at 298 K. Data for crystal-structure determination were collected by omega and phi scans. Data reduction was performed using the *APEX3* v2018.7-2 software package. An empirical absorption correction was applied using the *SADABS* 2016/2 program. The structure was solved using *SHELXT* 2018/2 (Sheldrick, 2015) and finally refined by full-matrix least-squares method based on  $F^2$  by *SHELXL2018/3* (Sheldrick, 2015). Neutral atom-scattering curves were used. All non-hydrogen atoms were anisotropically refined. Hydrogen atom positions were included in the model based on difference-Fourier electron density maps and refined without geometric constraints. Experimental details and cell parameters are given in Table 2. The crystallographic information file has been deposited with the Principal Editor of *Mineralogical Magazine* and is available as Supplementary material (see below). The bond valence analysis was performed using the most recent values of the bond valence parameters included in the 'bvparm2020.cif' data set from the International Union of Crystallography [https://www.iucr.org/], following the methodology of Witzke *et al.* (2000) and Brown (2006).

**Table 2.** Single-crystal XRD experimental details for ermelioite.

<b>Crystal data</b>	
Ideal formula	AlPO <sub>4</sub> ·H <sub>2</sub> O
Crystal dimensions (mm)	0.05 × 0.04 × 0.03
Crystal system, Space group	Monoclinic, C2/c
Temperature (K)	298(2)
$a, b, c$ (Å)	6.5371(4), 7.5670(5), 7.1146(5)
$\beta$ (°)	115.335(2)
$V$ (Å <sup>3</sup> )	318.08(4)
$Z$	4
Calculated density (g cm <sup>-3</sup> )	2.92
$\mu$ (mm <sup>-1</sup> )	1.009
<b>Data Collection</b>	
Crystal description	Prismatic, transparent, light blue
Instrument	Bruker D8 Venture Photon III 14
Radiation type, wavelength (Å)	MoK $\alpha$ , 0.71073
$\theta$ range (°)	4.38 to 28.29
Absorption correction	Multi-scan Bruker <i>Sadabs</i> -2016/2
$T_{min}, T_{max}$	0.873, 0.959
No. of measured, independent and observed [ $>2\sigma$ ] reflections	3116, 397, 367
$R_{int}$	0.031
Data completeness to 30.5° $\theta$ (%)	100
Indices range of $h, k, l$	-7 ≤ $h$ ≤ 8, -10 ≤ $k$ ≤ 10, -9 ≤ $l$ ≤ 9
<b>Refinement</b>	
Refinement method	Full-matrix least squares on $F^2$
Number of reflections, parameters, restraints	397, 39, 0
$R_1$ [ $I > 2\sigma(I)$ ], $R_1$ (all)	0.0209, 0.0235
$wR_2$ [ $I > 2\sigma(I)$ ], $wR_2$ (all)	0.0503, 0.0513
GoF	1.21
No. of refined parameters	39
$\Delta\rho_{max}$ (e <sup>-</sup> Å <sup>-3</sup> )/ $\Delta\rho_{min}$ (e <sup>-</sup> Å <sup>-3</sup> )	0.32/-0.4

$$R_{int} = \frac{\sum |F_o^2 - F_c^2|}{\sum F_o^2}, \text{ GoF} = S = \left\{ \frac{\sum [w(F_o^2 - F_c^2)]^2}{(n-p)} \right\}^{1/2}, R_1 = \frac{\sum |F_o - |F_c||}{\sum F_o}, wR_2 = \left[ \frac{\sum [w(F_o^2 - F_c^2)]^2}{\sum [w(F_o^2)]^2} \right]^{1/2}, w = 1/[\sigma^2(F_o^2) + (aP)^2 + bP] \text{ where } a \text{ is } 0.0057, b \text{ is } 1.0188 \text{ and } P \text{ is } [F_o^2 + 2F_c^2]/3.$$

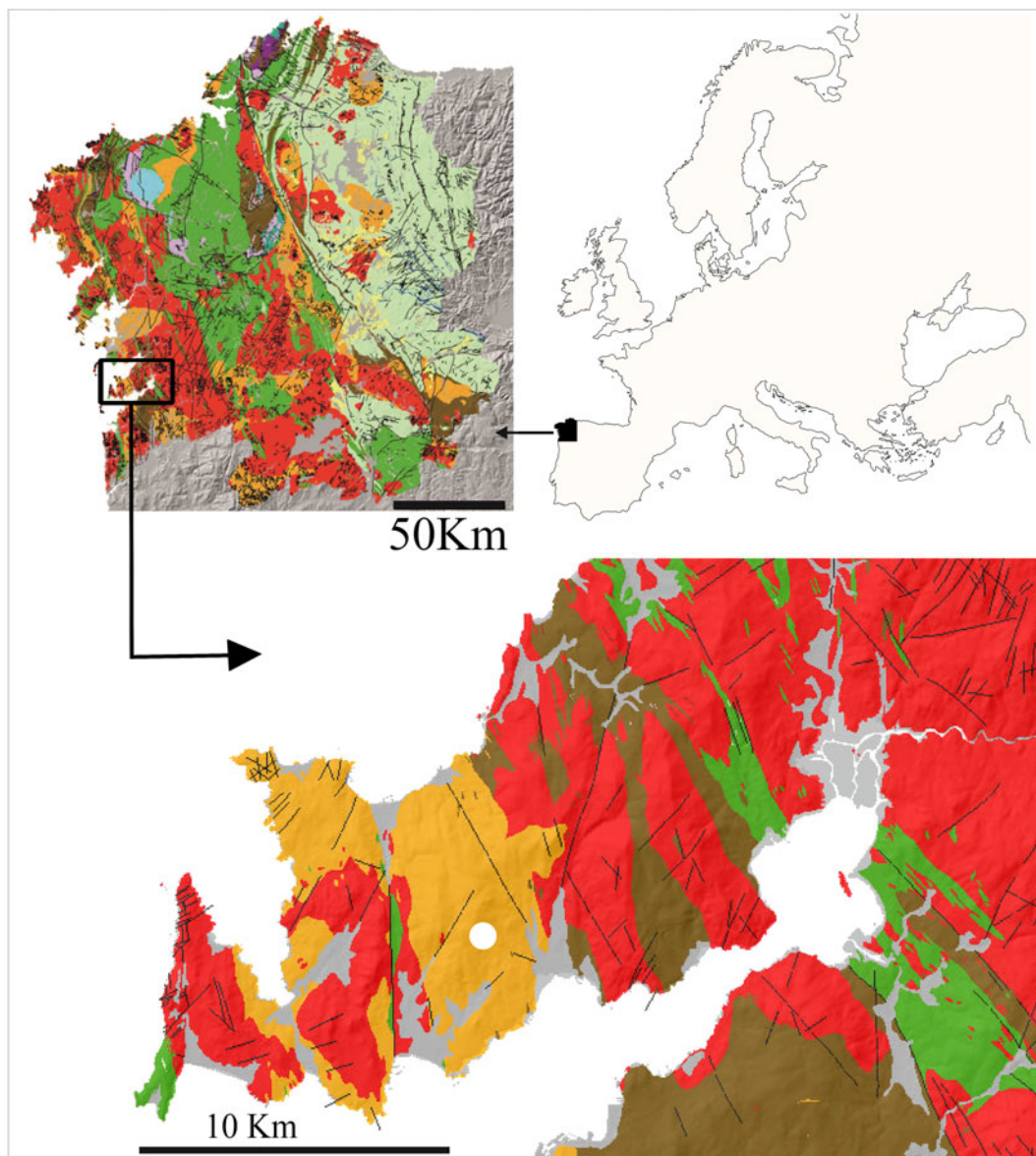


**Figure 1.** Geographical location and geological context of ermeoite. Top right: Galicia (black area) in Europe. Top left: Galicia and its geology. Below: magnified area showing the Morrazo peninsula and its geology. Orange: granodiorite with feldspar megacrystals (pegmatite with the ermeoite). Brown: biotitic gneiss. Green: mica-schists and paragneiss with plagioclase and biotite. Pale green: schists and quartzites. Red: alkaline feldspar granite. Grey: quaternary deposits. White: Atlantic Ocean. White dot: ermeoite location.

## Occurrence

The intrusive suite of granodiorites of the Morrazo peninsula are part of the Bayo–Vigo Massif. At the centre of this area is the Festiñazo granodiorite (Fig. 1), which consists of potassium feldspar megacrystals (3–4 cm) inside a matrix of fine- to medium-grained plagioclase, quartz, biotite and muscovite (Gallastegui Suárez, 2005). Within these granodiorites, decimetric to metric pegmatitic dykes occur, which are probably associated genetically to nearby two-mica granites (Rubio Navas, 1981; Gallastegui Suárez, 2005).

The pegmatite in which the ermeoite appears does not present miarolitic cavities or textural zonation. The main rock-forming minerals include quartz, microcline, albitic plagioclase, biotite, muscovite and occasionally some primary Fe/Mn phosphates.

Hydrothermal alteration has produced secondary minerals with variable contents of (OH) and H<sub>2</sub>O (heterosite, trolleite, crandalite, fluorapatite, rockbridgeite–frondelite, jahnsite-(CaMnMn), wardite, burangaite, mitridatite, phosphosiderite–strengite and cacoxenite). The sample of ermeoite studied is an ovoid nodule measuring 17.5 × 11.1 mm, embedded in albitic plagioclase.

The mineral occurs as short-prismatic crystals with a maximum size of 0.05 mm (Fig. 2). The colour of the mineral ranges from light blue to white and the streak is white. The crystals have a vitreous to pearly lustre and are transparent in thin fragments. Ermeoite is brittle and shows a conchoidal fracture. Mohs hardness is 3.5–4. The calculated density is 2.923 g/cm<sup>3</sup>. No fluorescence was detected under ultraviolet light. Optical properties could not be measured due to the microgranular nature of the specimen (Supplementary Fig. S2).

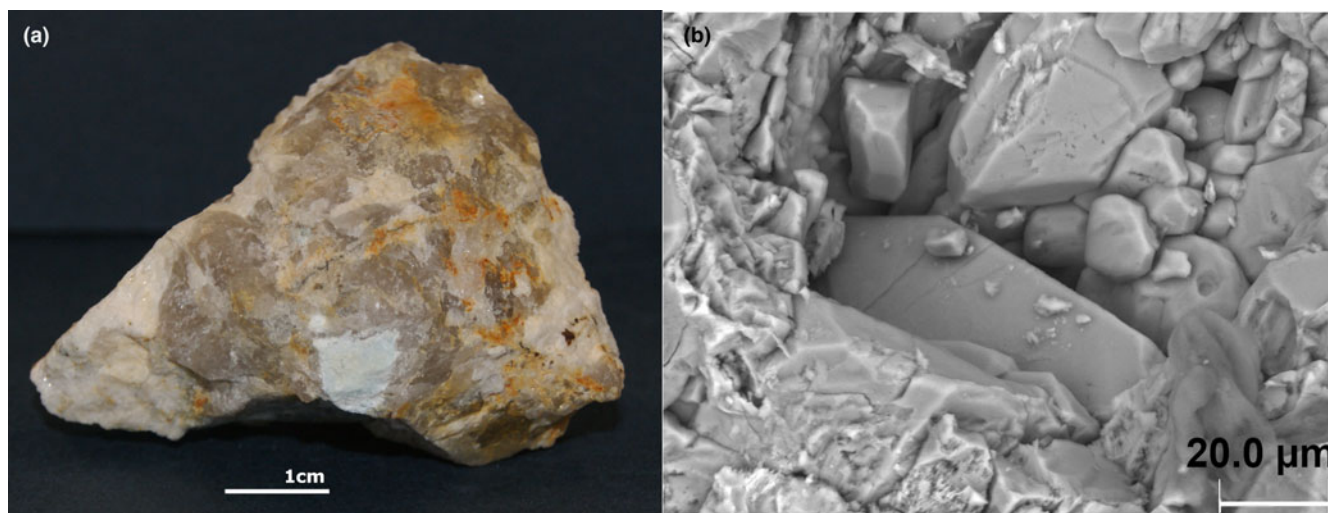


**Figure 2.** (a) Light blue aggregated crystals of ermeloite embedded in albitic plagioclase. Museo de Historia Natural of the University of Santiago de Compostela registration number (CMG4083). (b) Scanning electron microscope image of ermeloite crystalline mass.

## Results and discussion

### Composition

The results of the EMPA of ermeloite are presented in Table 3. The empirical formula obtained from the chemical analysis is  $\text{Al}_{1.022}\text{Fe}_{0.002}\text{K}_{0.003}\text{P}_{0.950}\text{F}_{0.055}\text{H}_{2.120}\text{O}_{4.950}$ . The simplified formula is  $\text{Al}_{1.02}\text{P}_{0.95}\text{F}_{0.06}\text{O}_{3.88}\cdot 1.06\text{H}_2\text{O}$  (elements present in amounts  $<0.01$  apfu have not been included in the simplified formula). This simplified formula is close to the ideal formula  $\text{AlPO}_4\cdot\text{H}_2\text{O}$ . The water content has been calculated by difference, and it is in agreement with crystallographic data.

### Raman spectroscopy

The Raman spectrum of ermeloite was recorded between 100 and  $3700\text{ cm}^{-1}$  (Fig. 3). In the region above  $1200\text{ cm}^{-1}$ , it shows a weak intensity band at  $1542\text{ cm}^{-1}$ , trapezoidal bands in the  $2100\text{--}2800\text{ cm}^{-1}$  region, and broad bands centred at  $3150$  and  $2996\text{ cm}^{-1}$ . These bands were tentatively assigned on the basis of literature data for related compounds. For example, in Kieserite-type compounds, bands at  $1500\text{ cm}^{-1}$  and  $3100\text{--}3400\text{ cm}^{-1}$  are reported as  $\nu_2$  bending and  $\nu_1, \nu_3$  stretching modes of  $\text{H}_2\text{O}$  (Wang *et al.*, 2006; Talla and Widner, 2019 or Chio, 2007). Bands around  $2800\text{ cm}^{-1}$  in the IR spectrum were assigned to  $\nu(\text{MnO-H})$  or  $\nu(\text{H}_3\text{O}^+)$  in serrabrancaite (Aranda and Bruque, 1990) and (Boonchom *et al.*, 2008), but these Raman spectroscopy techniques are highly sensitive to organic impurities, which result in characteristic C–H bond vibrations in

the  $2800\text{--}3000\text{ cm}^{-1}$  and  $1400\text{--}1500\text{ cm}^{-1}$  regions, (Redkov *et al.*, 2019 and references cited therein). Therefore, the assignment of these bands for cases involving natural systems is a matter of debate in the specialised literature.

In the region below  $1200\text{ cm}^{-1}$ , the Raman shift is in good agreement with spectral bands obtained by other authors (Breitinger *et al.*, 2004; Frost *et al.*, 2004, 2014) for different phosphate minerals such as variscite, phosphosiderite, or wardite. Three bands at  $1126, 1080$  and  $1008\text{ cm}^{-1}$  are present in the Raman  $\nu_1$  symmetric and  $\nu_3$  antisymmetric stretching region ( $900\text{--}1200\text{ cm}^{-1}$ ) of  $\text{PO}_4^{3-}$ . Bands at  $617, 514$  and  $427\text{ cm}^{-1}$  can be assigned to  $\nu_4$  out-of-plane and  $\nu_2$  in-plane bending modes of phosphates. Finally, the Raman spectrum of ermeloite in the  $180\text{--}350\text{ cm}^{-1}$  region shows a strong intense band near  $317\text{ cm}^{-1}$ , and two others at  $257$  and  $187\text{ cm}^{-1}$ . Raman bands below  $300\text{ cm}^{-1}$  reported in the literature are related to the O–M–O skeleton vibrational modes, such as the Al–O stretching mode at  $326\text{ cm}^{-1}$  in variscite or metavariscite or the O–M–O symmetric bending mode of strengite at  $193\text{ cm}^{-1}$  and variscite at  $230\text{ cm}^{-1}$  (Frost *et al.*, 2014).

### Crystal structure

Single-crystal XRD shows that ermeloite crystallises in the monoclinic space group  $C2/c$  with cell parameters  $a = 6.5371(4)\text{ \AA}$ ,  $b = 7.5670(5)\text{ \AA}$ ,  $c = 7.1146(5)\text{ \AA}$ ;  $\beta = 115.335(2)^\circ$ ,  $V = 318.08(4)\text{ \AA}^3$  and  $Z = 4$ . Atomic positions are given in Table 4.

Ermeloite presents a kieserite-type structure constructed of kinked chains of corner-sharing  $\text{AlO}_6$  elongated octahedrons along  $[101]$ , where the shared O3 oxygen atom is part of an  $\text{H}_2\text{O}$  molecule. These chains are further connected by regular  $\text{PO}_4$  tetrahedra through the O2 oxygen atoms, forming chains cross-link with adjacent chains, to form a mixed tetrahedral–octahedral framework through O1 atoms (Fig. 4b). These structural arrangements are stabilised by hydrogen bonds between O3 and adjacent O2 atoms along the  $a$  axis (Fig. 4d).

Bond distances and angles for octahedral and tetrahedral units are reported in Table 5. The average  $\langle\text{P-O}\rangle$  bond lengths ( $1.5303\text{ \AA}$ ) and  $\langle\text{O-P-O}\rangle$  angles ( $109.47^\circ$ ) indicate that the phosphate

**Table 3.** Compositional data ( $n = 18$ ) for ermeloite expressed as oxides wt.%.

Constituent	Mean	Range	S.D. ( $\sigma$ )	Probe standard
$\text{Al}_2\text{O}_3$	37.360	38.591–36.284	0.633	Albite <sup>2</sup>
FeO	0.079	0.136–0.042	0.027	Almandine <sup>1</sup>
$\text{K}_2\text{O}$	0.108	0.157–0.048	0.035	Microcline <sup>1</sup>
$\text{P}_2\text{O}_5$	48.330	49.153–47.622	0.442	Fluorapatite <sup>1</sup>
F	0.755	0.981–0.576	0.117	Fluorapatite <sup>1</sup>
$\text{F}\equiv\text{O}$	–0.318	–0.242/–0.413	0.049	–
$\text{H}_2\text{O}$ (*)	13.69	15.314–11.561	1.014	–
Total	100.00			

S.D. – standard deviation; \*by difference.

<sup>1</sup>Jarosewich *et al.* (1980); <sup>2</sup>McGuire *et al.* (1992).

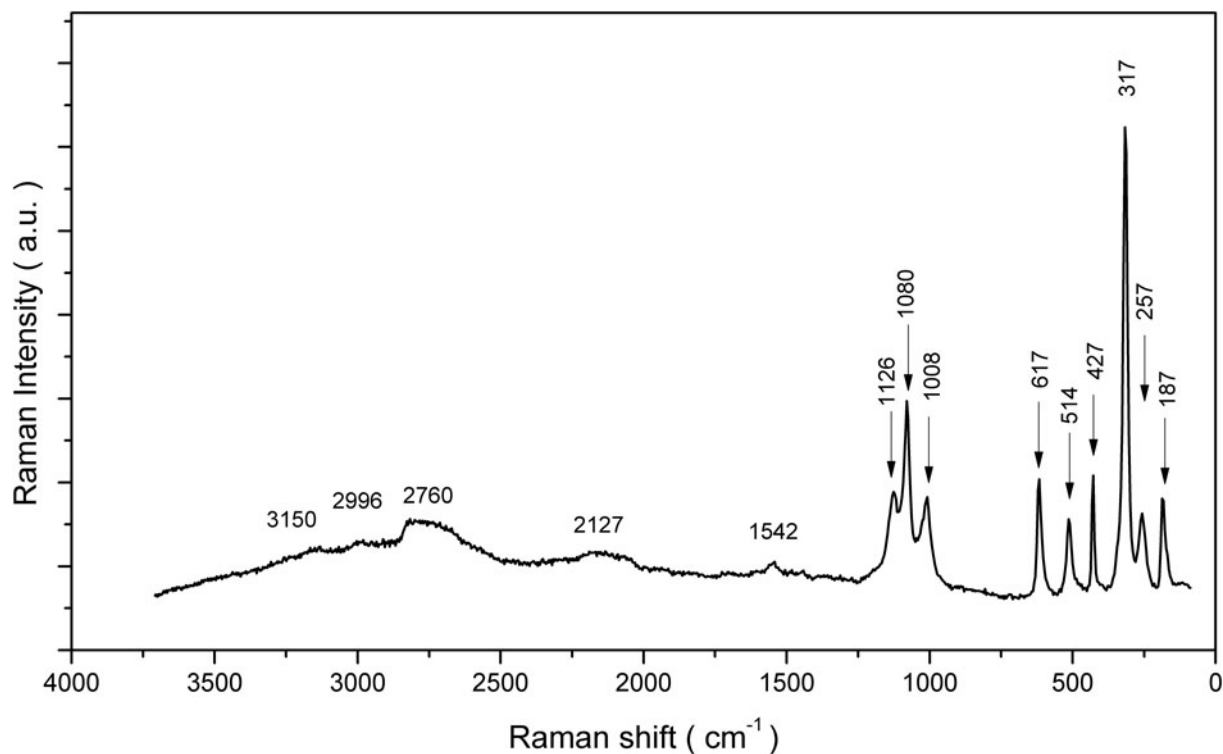


**Figure 3.** Raman spectrum of ermeloite using a randomly oriented crystal.

tetrahedron is quite regular, in good agreement with the value obtained by Baur (1974) ( $\langle P-O \rangle = 1.537 \text{ \AA}$ ) and confirmed by Huminicki and Hawthorne (2019) for minerals containing ( $P\phi_4$ ) tetrahedra. The observed P–O2 distance ( $1.5454(14) \text{ \AA}$ ) is typical of a single P–O bond ( $1.546 \text{ \AA}$ ), whereas the P–O1 distance ( $1.5152(14) \text{ \AA}$ ) is significantly shorter than a single bond and slightly longer than a double P=O bond ( $1.504 \text{ \AA}$ ), thereby indicating a delocalisation of the charge along O1–P–O1.

The aluminium atoms are [2+2+2] coordinated with four phosphates in an equatorial plane (through O1 and O2) and two  $H_2O$  molecules (O3) in axial positions (Fig. 4c). According to Schindler and Hawthorne (1999), the only way to stabilise [ $M^{3+}(T^{5+}O_4)(H_2O)$ ] structures in the kieserite group arrangement, and for the  $M^{3+}-O_3-M^{3+}$  linkage to occur, require an elongation of the  $M^{3+}-O_3$  bonds to make the incident bond valence sums around the bridging anion compatible. The  $Al^{3+}$  cation has a  $3d^0$  electronic configuration, like  $Mg^{2+}$ , but the required elongation, is greater in trivalent compounds than in divalent ones, as is evidenced in Supplementary Fig. S3.  $Mn^{3+}$  and  $V^{3+}$  have  $M-O_3$  bond lengths similar to bulkier  $M^{2+}$  cations, and at least  $0.1 \text{ \AA}$  greater than would be expected for a divalent cation with the same ionic radius. This large elongation requirement makes it surprising that the  $AlPO_4 \cdot H_2O$  species crystallises

in a Kieserite-type structure, as the cation lacks a specific electron mechanism to induce the required elongation.

The compatibility of this  $Al^{3+}-O_3-Al^{3+}$  arrangement in the kieserite-type structure, with bond valence sums in the ermeloite, can be observed in Table 6. The structure compensates for the deficiencies in the formal incident bond valence sums mainly by shortening the bonds to O1 and lengthening those to O3. This can be observed in the largest Al–O3 distance ( $2.0509(9) \text{ \AA}$ ) compared to Al–O2 ( $1.8662(13) \text{ \AA}$ ) and Al–O1 ( $1.8158(13) \text{ \AA}$ ). These values differ significantly from the Al–O bond distances recorded in the CCDC database (Cambridge Crystallographic Data Centre, <https://www.ccdc.cam.ac.uk/>) for  $AlO_6$  (Supplementary Fig. S4). The corresponding bond angles, O1–Al–O2, O1–Al–O3 and O2–Al–O3, are  $87.13(6)^\circ$ ,  $88.13(4)^\circ$  and  $87.14(6)^\circ$ , respectively. These angles represent deviations of less than  $2.9^\circ$  from the ideal angles. Interestingly, the elongation of the Al–O3 bond occurs without significant alterations in the octahedral angles. This phenomenon may be facilitated by the presence of a square-plane in the equatorial position, formed by four different phosphates (Fig. 4d), resulting in a relatively low-tension octahedral configuration, which is further evidenced by a high quadratic elongation value ( $1.008$ ), despite the relatively low variance in octahedral angles ( $7.23 \text{ deg}^2$ ). Similar trends were also observed

**Table 4.** Atomic coordinates and displacement parameters.

Site	$x/a$	$y/b$	$z/c$	$U_{eq}$	$U^{11}$	$U^{22}$	$U^{33}$	$U^{23}$	$U^{13}$	$U^{12}$
Al	$\frac{1}{4}$	$\frac{3}{4}$	$\frac{1}{2}$	0.0108(2)	0.0120(4)	0.0099(4)	0.0121(4)	0.0008(3)	0.0068(3)	0.0014(3)
P	$\frac{1}{2}$	0.58251(9)	$\frac{1}{4}$	0.0092(2)	0.0096(3)	0.0088(3)	0.0102(3)	0	0.0052(3)	0
O1	0.4619(2)	0.69597(18)	0.4076(2)	0.0119(3)	0.0122(6)	0.0116(6)	0.0137(7)	–0.0020(5)	0.0071(6)	–0.0002(5)
O2	0.2892(2)	0.46405(18)	0.1416(2)	0.0121(3)	0.0114(6)	0.0107(6)	0.0147(7)	–0.0021(5)	0.0060(5)	–0.0012(5)
O3	0	0.6275(3)	$\frac{1}{4}$	0.0120(4)	0.0115(9)	0.0141(9)	0.0116(9)	0	0.0061(8)	0
H	–0.073(5)	0.559(4)	0.293(5)	0.043(9)	–	–	–	–	–	–

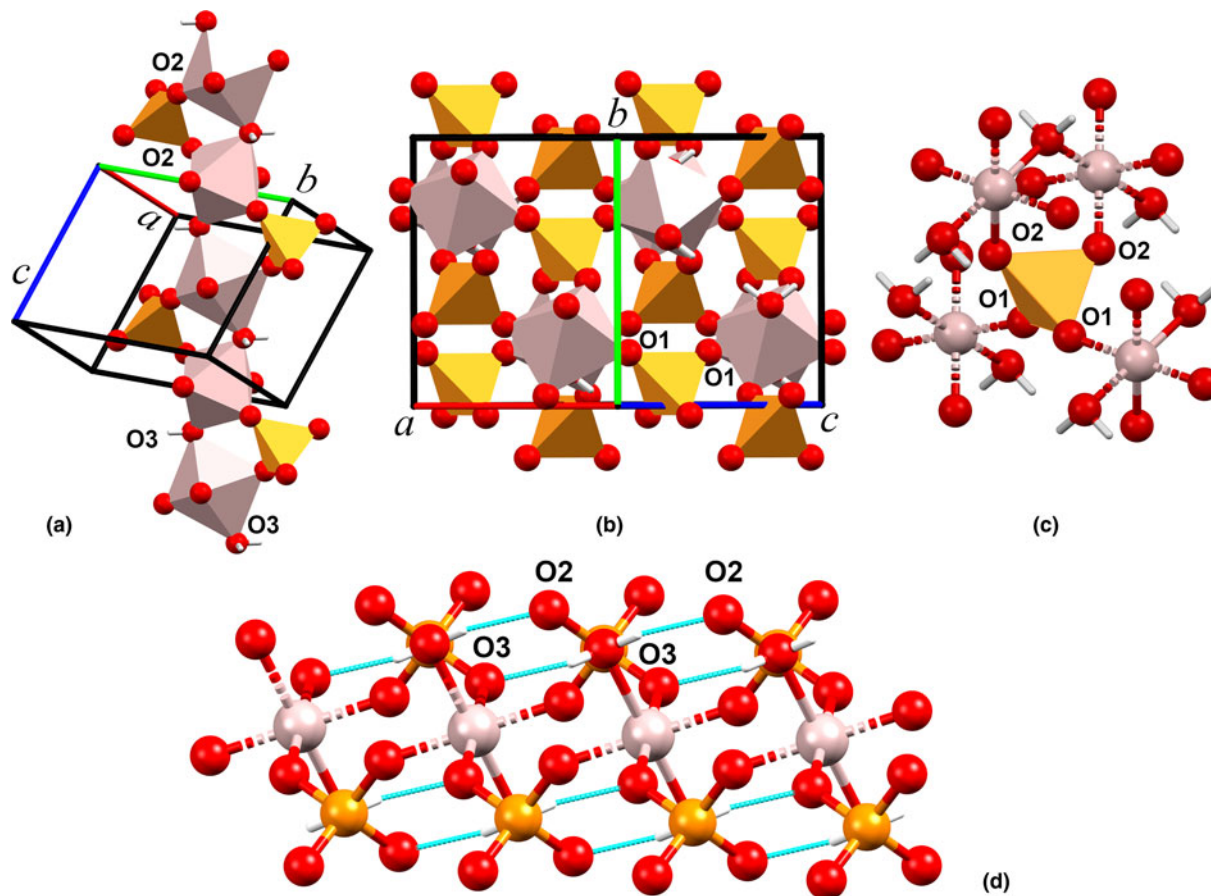


**Figure 4.** Structure of ermeloite: (a) corner-sharing ( $\text{AlO}_6$ )-octahedral chain along [101] direction; (b) mixed tetrahedral- octahedral ( $\text{PO}_4$ - $\text{AlO}_6$ ) framework; (c) cation octahedral detail; (d) H-bond interactions. Drawn using CCDC *Mercury* software.

for other isostructural phosphates (Supplementary Fig. S5). This behaviour differs from the general observations reported by Robinson *et al.* (1971) for different cations in different families of minerals, such as olivines, humites, garnets, amphiboles, pyroxenes, etc. For divalent kieserites (sulfates and selenates) an intrinsic value of the elongation is observed but the octahedral distortion is lower than for phosphates (Supplementary Fig. S5).

The corner-sharing octahedral chains have an angular relationship of  $126.25(10)^\circ$  between consecutive octahedrons ( $M\text{-O}3\text{-}M$ ). In addition, they feature angles of  $141.98(9)^\circ$  and  $131.30(8)^\circ$  with respect to adjacent chains, as determined by the  $\text{Al-O}1\text{-P}$  and  $\text{Al-O}2\text{-P}$  angles, respectively. Finally, the refined bond distances  $\text{O}3\text{-H} = 0.84(3)\text{\AA}$  and the dihedral angle  $\text{H-O}3\text{-H} = 104(4)^\circ$  of the water molecule present appropriate values,

and the strong hydrogen bonding interactions are evidenced by the short  $\text{O}3\cdots\text{O}2$  distance ( $2.6356(17)\text{\AA}$ ).

#### Relationship with isostructural phosphates

The new mineral ermeloite is isostructural with kieserite-type compounds of general stoichiometry  $[\text{M}(\text{TO}_4)\cdot(\text{H}_2\text{O})]$  ( $M = \text{Mg}^{2+}$ ,  $\text{Fe}^{2+}$ ,  $\text{Ni}^{2+}$ ,  $\text{Co}^{2+}$ ,  $\text{Mn}^{2+}$  and  $\text{Zn}^{2+}$ ;  $T = \text{S}$  and  $\text{Se}$ ) (Leonhardt and Weiss, 1957; Bregeault *et al.*, 1970, Wildner and Giester, 1991) and two other phosphates ( $M = \text{Mn}^{3+}$  and  $\text{V}^{3+}$ ;  $T = \text{P}$ ): serrabrancaite  $\text{MnPO}_4\cdot\text{H}_2\text{O}$  (Lightfoot *et al.*, 1987; Witzke *et al.*, 2000) and synthetic  $\text{VPO}_4\cdot\text{H}_2\text{O}$  (Vaughey *et al.*, 1994).

For better comparison with ermeloite, a unit cell transformation was performed to orientate the structure like kieserite,

**Table 5.** Selected interatomic distances ( $\text{\AA}$ ) and angles ( $^\circ$ ) for  $[\text{AlPO}_4\cdot\text{H}_2\text{O}]$ .

$\text{Al-O}1^{\text{ii,iii}}$ $\times 2$	1.8158(13)	$\text{O}1^{\text{ii}}\text{-Al-O}1^{\text{iii}}$	180	$\text{O}2\text{-P-O}2^{\text{v}}$	109.09(11)
$\text{Al-O}2^{\text{i,iii}}$ $\times 2$	1.8662(13)	$\text{O}2^{\text{i}}\text{-Al-O}2^{\text{iv}}$	180	$\text{O}1^{\text{iv}}\text{-P-O}2^{\text{iv}}$ $\times 2$	107.72(7)
$\text{Al-O}3^{\text{i,iii}}$ $\times 2$	2.0509(9)	$\text{O}3^{\text{iv}}\text{-Al-O}3$	180	$\text{O}1^{\text{iv}}\text{-P-O}2^{\text{vi}}$ $\times 2$	110.67(7)
$\langle\text{Al-O}\rangle$	1.9110			$\text{O}1\text{-P-O}1$	110.97(11)
		$\text{O}1^{\text{iii,ii}}\text{-Al-O}2^{\text{iv}}$ $\times 2^{\text{a}}$	87.13(6)	$\langle\text{O-P-O}\rangle$	109.47
$\text{P-O}1^{\text{i,v}}$ $\times 2$	1.5152(14)	$\text{O}1^{\text{iii,iv}}\text{-Al-O}3^{\text{iv}}$ $\times 2^{\text{a}}$	88.13(4)		
$\text{P-O}2^{\text{i,v}}$ $\times 2$	1.5454(14)	$\text{O}2^{\text{iv}}\text{-Al-O}3^{\text{iv,i}}$ $\times 2^{\text{a}}$	87.14(6)	$\text{O}3\text{-H}$	0.84(3)
$\langle\text{P-O}\rangle$	1.5303	$\langle\text{O-Al-O}\rangle$	90	$\text{H-O}3\text{-H}$	104(4)
		$\text{Al-O}3\text{-Al}^{\text{v}}$	126.25(10)	$\text{O}3\text{-H}\cdots\text{O}2^{\text{v}}$	2.6356(17)

<sup>a</sup>plus 2 $\times$  corresponding obtuse angles. Symmetry codes: (i)  $x,y,z$ ; (ii)  $x-\frac{1}{2}, -y+\frac{1}{2}, z-\frac{1}{2}$ ; (iii)  $-x+\frac{1}{2}, y+\frac{1}{2}, -z+\frac{1}{2}$ ; (iv)  $-x, -y+1, -z$ ; (v)  $-x, y, -z+\frac{1}{2}$ ; (vi)  $-x+\frac{1}{2}, y-1/2, -z+\frac{1}{2}$ .

**Table 6.** Bond valence analysis (valence units) for ermeloite.\*

	Al	P	H	$\Sigma$
O(1)	0.640 <sup>x2↓</sup>	1.317 <sup>x2↓</sup>		1.957
O(2)	0.559 <sup>x2↓</sup>	1.214 <sup>x2↓</sup>	0.255	2.028
O(3)	0.339 <sup>x2↓→</sup>		0.745 <sup>x2→</sup>	2.168
$\Sigma$	3.077	5.062	1	

\*Bond valence analysis was made with latest values of bond valence parameters included in 'bvpam2020.cif' data set from the International Union of Crystallography [https://www.iucr.org/], following the methodology of Witzke *et al.* (2000) and Brown (2006).

with octahedral chains along [001] (Fig. S6). New crystallographic settings ( $a'$ ,  $b'$ ,  $c'$ ,  $\beta'$ ) will be used, to refer to this new orientation.

### Influence of the ionic radius of cations

The influence of the ionic radius of divalent cations on structural parameters (bond distances and angles) and cell dimensions (volume, axial lengths, or cell angles) has been analysed previously for kieserite-group sulfates ( $T=S$ ) (Hawthorne *et al.*, 1987; Wildner and Giester, 1991) and isostructural selenates ( $T=Se$ ) (Giester and Wildner, 1992). These works provided evidence of a gradual variation in the crystallographic axes  $a'$  and  $c'$ , while the  $b'$  axis and the  $\beta'$  angle showed only minor deviations.

In the phosphates examined, notably distinct values were observed for the  $b'$  axis, together with significant variations in all the cell parameters in the case of serrabrancaite. However, when analysing Fig. 5a,b, in particular the cases of  $V^{3+}$  and  $Mn^{3+}$  (with similar ionic radius), the data suggest that all the variations in cell dimensions are produced so that the overall volume

of the unit cell adapts to the ionic radius of the cation. Significant differences in the Mn–O bond distances were also observed in the case of serrabrancaite (Fig. 5d), possibly stemming from an increased  $M-O3$  elongation due to the well-known Jahn-Teller effect (high-spin  $t_{2g}^3 e_g^1$  configuration) in  $Mn^{3+}$  (Burns *et al.*, 1994), but overall, an increase in ionic radius leads to a linear rise in the average  $\langle M-O \rangle$  bond lengths, in agreement with Kuppuraj *et al.* (2009). Consequently, this increase is reflected in the polyhedral volume, as depicted in Fig. 5c. The pronounced elongation of the O3 direction in phosphates is counterbalanced by a reduction in  $M-O2$  and (especially)  $M-O1$  distances to maintain an appropriate octahedral volume.

The P–O–M bond angles between adjacent chains range from  $137^\circ$  ( $M=V^{3+}$ ) to  $142^\circ$  ( $M=Al^{3+}$ ) for O1 and from  $129^\circ$  ( $M=V^{3+}$ ) to  $135^\circ$  ( $M=Mn^{3+}$ ) for O2. This implies greater variations in bond angles compared to sulfates and selenates, which show variations of  $\sim 1^\circ$  for O1 and  $3^\circ$  for O2. Furthermore, these angles do not increase smoothly with the size of the cation, as observed for divalent compounds, except for  $Mg^{2+}$  (Fig. 5e). In contrast, the  $M-O3-M$  angle decreases with the ionic radius of the cations, aligning with expected behaviour.

### Relationship between cell axis lengths and geometric parameters

Factors that influence the length of cell parameters are difficult to identify in the case of the isostructural phosphates ermeloite, serrabrancaite, and synthetic  $VPO_4 \cdot H_2O$ , as only three compounds can be compared. Hence, definitive conclusions cannot be drawn. However, those that might have a logical relationship and a reasonable trend have been analysed. The main

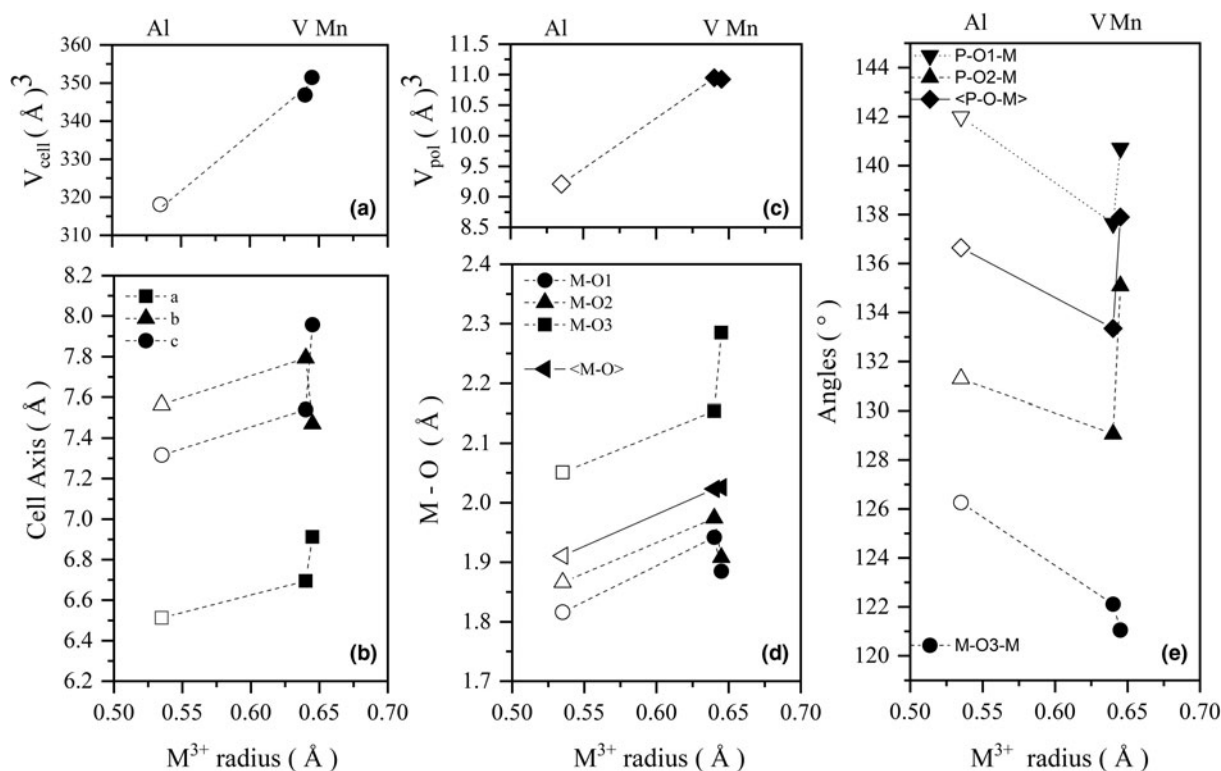


**Figure 5.** Influence of cation ionic radius on the cell and structural parameters for ermeloite and isostructural phosphates, (a) cell volume, (b) cell axis, (c) polyhedral volume, (d) bond lengths, (e) P–O–M and M–O3–M angles. Ermeloite (open symbol).

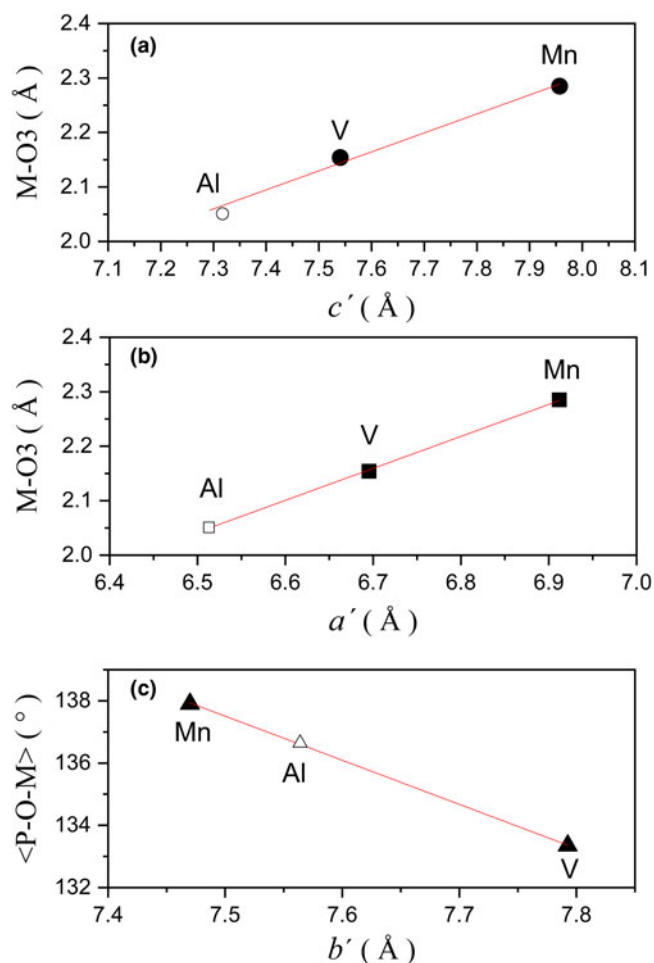


**Figure 6.** Relationship between cell axis lengths and geometric parameters for ermeloite and isostructural phosphates, (a)  $c'$  axis vs.  $M-O3$  bonds, (b)  $a'$  axis vs.  $M-O3$  bonds, (c) average  $P-O-M$  angle vs.  $b'$ . Ermeloite (open symbol).

characteristic of these compounds is their long  $M-O3$  bond. This elongation occurs along the  $c'$  axis. It is therefore reasonable to infer that the  $c'$  axis parameters observed in phosphates are associated with the significant elongation of the  $M-O3$  bonds, as depicted in Fig. 6a. Similarly, the  $a'$  axis also appears to exhibit an almost linear behaviour with the elongation of  $M-O3$  (Fig. 6b). This could be due to the relative positions of the phosphate anion and the  $H_2O$  molecule involved in the H-bonds between O3 and O2 along the  $a'$  axis. Finally, a reverse effect on the  $b'$  axis is observed with increasing  $M-O-P$  angle (Fig 6c). Giester and Wildner (1992) attributed differences in cell axis dimensions between sulfates and selenates to a variation in  $M-O-T$  angles caused by anion rotations around the  $b'$  axis. Interestingly, a linear relationship between these angular values is maintained in the three phosphates studied.

## Conclusions

Ermeloite, a new phosphate mineral with the ideal formula  $AlPO_4 \cdot H_2O$ , has been discovered in Chans de Ermelo, Galicia, Spain. It is the third new mineral species discovered in Galicia. It is monoclinic and crystallises in the  $C2/c$  space group with cell parameters  $a = 6.5371(4)$  Å,  $b = 7.5670(5)$  Å,  $c = 7.1146(5)$  Å;  $\beta = 115.335(2)^\circ$ ,  $V = 318.08(4)$  Å<sup>3</sup> and  $Z = 4$ . The mineral has a

kieserite-type structure, showing that cations such as  $Al^{3+}$  with the formula  $[M^{3+}(T^{5+}O_4)(H_2O)]$  and without  $d$  orbitals or the Jahn-Teller effect, can be present in members of this structural type.

Comparisons of crystallographic data show significant variations between serrabrancaite  $MnPO_4 \cdot H_2O$  and the isostructural phosphates ermeloite and  $VPO_4 \cdot H_2O$ . However linear relationships were observed for the two unit cell parameters (oriented as kieserite)  $a'$  and  $c'$  with  $M-O3$  bond lengths, while  $b'$  showed an inverse linear relationship with increasing  $M-O-P$  angle. Unfortunately, with only three data points, these trends cannot be truly established.

**Acknowledgements.** The authors would like to thank Moisés Núñez and Manuel Cerviño for their contribution to this discovery and Dr. Antonio L. Llamas-Saiz and Prof Lionel Delaude for revising the manuscript. This research was funded by the Área de Infraestructuras de Investigación of the Universidade de Santiago de Compostela (USC). All the analyses were carried out at the Área de Infraestructuras de Investigación (USC) except for the EMPA, which was done with the assistance of Alfredo Fernández Larios, at the Centro de Microscopía Electrónica, Universidad Complutense (Madrid, Spain). We appreciate the efforts of the reviewers and editors to improve this article.

**Supplementary material.** The supplementary material for this article can be found at <https://doi.org/10.1180/mgm.2024.33>.

**Competing interests.** The authors declare none.

## References

- Aranda M.A.G. and Bruque S. (1990) Characterization of manganese(III) orthophosphate hydrate. *Inorganic Chemistry*, **29**, 1334–1337.
- Baur W.H. (1974) The geometry of polyhedral distortions. Predictive relationships for the phosphate group. *Acta Crystallographica*, **B30**, 1195–1215.
- Boonchom B., Youngme S., Maensiri S. and Danvirutai C. (2008) Nanocrystalline serrabrancaite ( $MnPO_4 \cdot H_2O$ ) prepared by a simple precipitation route at low temperature. *Journal of Alloys and Compounds*, **454**, 78–82.
- Bregeault J.M., Herpin J.M., Manoli J.M. and Pannetier G. (1970) Affinement de la structure de la Kieserite  $MgSO_4 \cdot H_2O$ . *Bulletin de la Société Chimique de France*, **12**, 4243–4248.
- Breitinger D.K., Belz H.-H., Hajba L., Komlósi V., Mink J., Brehm G., Colognesi D., Parker S.F. and Schwab R.G. (2004) Combined vibrational spectra of natural wardite. *Journal of Molecular Structure*, **706**, 95–99.
- Brown I.D. (2006) *The Chemical Bond in Inorganic Chemistry: The Bond Valence Model*. International Union of Crystallography Monographs on Crystallography. Oxford University Press, Oxford, UK, 292 pp.
- Burns P.C., Cooper M.A. and Hawthorne F.C. (1994) Jahn-Teller-distorted  $Mn^{3+}O_6$  octahedra in fredrikssonite, the fourth polymorph of  $Mg_2 Mn^{3+}(BO_3)_2O_2$ . *The Canadian Mineralogist*, **32**, 397–403.
- Chio C.H., Sharma S.K. and Muenow D.W. (2007) The hydrates and deuterates of ferrous sulfate ( $FeSO_4$ ): a Raman spectroscopic study. *Journal of Raman Spectroscopy*, **38**, 87–99.
- Degen T., Sadki M., Bron E., König U. and Nénert G. (2014) The HighScore suite. *Powder Diffraction*, **29**, S13–S18.
- Dufrénoy A. (1845) *Traité de Minéralogie*. Carilian Goevry et Vr. Dalmont Editeurs, Paris, vol 2. 654–655 pp.
- Frost R.L., Weier M.L., Erickson K.L., Carmody O. and Mills S.J. (2004) Raman spectroscopy of phosphates of the variscite mineral group. *Journal of Raman Spectroscopy*, **35**, 1047–1055.
- Frost R.L., Scholz R., López A., Lana C. and Xi Y. (2014) A Raman and infrared spectroscopic analysis of the phosphate mineral wardite  $NaAl_3(PO_4)_2(OH)_4 \cdot 2(H_2O)$  from Brazil. *Spectrochimica Acta Part A: Molecular and Biomolecular Spectroscopy*, **126**, 164–169.
- Gallastegui Suárez G. (2005) Petrología del Macizo granodiorítico de Bayo – Vigo (Provincia de Pontevedra, España). Tesis Doctoral Universidad de Oviedo. *Laboratorio Xeolóxico de Laxe, Serie Nova Terra*, **26**, 414. Edicións do Castro, Sada. A Coruña.

- Giester G. and Wildner M. (1992) The crystal structures of kieserite-type compounds. II. Crystal structures of  $\text{Me(II)SeO}_4 \cdot \text{H}_2\text{O}$  (Me = Mg, Mn, Co, Ni, Zn). *Neues Jahrbuch für Mineralogie Monatshefte*, **3**, 135–144.
- Hawthorne F.C., Groat L.A., Raudsepp M. and Ercit T.S. (1987) Kieserite,  $\text{MgSO}_4 \cdot \text{H}_2\text{O}$ , a titanite-group mineral. *Neues Jahrbuch für Mineralogie – Abhandlungen*, **157**, 121–132.
- Huminicki D.M.C. and Hawthorne F.C. (2019) The crystal chemistry of the phosphate minerals. *Phosphates: Geochemical, Geobiological and Materials Importance*, **48**, 123–254.
- Jarosevich E., Nelen J.A. and Norberg J.A. (1980) Reference Samples for Electron Microprobe Analysis. *Geostandards and Geoanalytical Research*, **4**, 43–47.
- Kuppuraj G., Dudev M. and Lim C. (2009) Factors governing metal–ligand distances and coordination geometries of metal complexes. *The Journal of Physical Chemistry B*, **113**, 2952–2960.
- Leonhardt J. and Weiss R. (1957) Das Kristallgitter des Kieserits  $\text{MgSO}_4 \cdot \text{H}_2\text{O}$ . *Die Naturwissenschaften*, **44**, 338–339.
- Lightfoot P., Cheetham A.K., Sleight A.W., Tayal V.P., Khandelwal D.P., Bist H.D., Redkov A., Melehin V., Zhurikhina V., Frost R.L., Weier M.L., Erickson K.L., Carmody O., Mills S.J., Petruševski V.M., Aleksovska S., Pluth J.J. and Smith J. V. (1987) Structure of  $\text{MnPO}_4 \cdot \text{H}_2\text{O}$  by synchrotron X-ray powder diffraction. *Inorganic Chemistry*, **26**, 3544–3547.
- Martínez Alcívar A. (1850) Raro e importante mineral de níquel. *Revista Minera*, **1**, 302–306.
- Martínez Alcívar A. (1851) Sobre el mineral de níquel de Galicia, con algunas consideraciones sobre el polimorfismo del sulfato de níquel y de otras sustancias. *Revista Minera*, **2**, 175–184.
- McGuire A.V., Francis C.A. and Dyar M.D. (1992) Mineral standards for electron microprobe analysis of oxygen. *American Mineralogist*, **77**, 1087–1091.
- Moore P.B. (1970) Crystal chemistry of the basic iron phosphates. *American Mineralogist*, **55**, 135–169.
- Redkov A., Melehin V. and Zhurikhina V. (2019) Is adsorbed water responsible for 2800–3000  $\text{cm}^{-1}$  band in Raman spectrum of inorganic matter? *Journal of Physics: Conference Series*, **1236**, 012001.
- Robinson K., Gibbs G.V. and Ribbe P.H. (1971) Quadratic elongation: A quantitative measure of distortion in coordination polyhedra. *Science (New York, N.Y.)*, **172**, 567–570.
- Rubio Navas J. (1981) *Memoria del Mapa Geológico de España a escala 1:50.000, Hoja 223 (Vigo)*. Madrid, 34 pp.
- Schindler M. and Hawthorne F.C. (1999) Schubnelite,  $[\text{Fe}^{3+}(\text{V}^{5+}\text{O}_4)(\text{H}_2\text{O})]$ , a novel heteropolyhedral framework mineral. *American Mineralogist*, **84**, 665–668.
- Sheldrick G.M. (2015) Crystal structure refinement with SHELXL. *Acta Crystallographica*, **C71**, 3–8.
- Talla D. and Wildner M. (2019) Investigation of the kieserite–szomolnokite solid-solution series,  $(\text{Mg,Fe})\text{SO}_4 \cdot \text{H}_2\text{O}$ , with relevance to Mars: Crystal chemistry, FTIR, and Raman spectroscopy under ambient and martian temperature conditions. *American Mineralogist*, **104**, 1732–1749.
- Vaughey J.T., Harrison W.T.A., Jacobson A.J., Goshorn D.P. and Johnson J.W. (1994) Synthesis, structure, and properties of two new vanadium(III) phosphates:  $\text{VPO}_4 \cdot \text{H}_2\text{O}$  and  $\text{V}_{1.23}(\text{PO}_4)(\text{OH})_{0.69}(\text{H}_2\text{O})_{0.31} \cdot 0.33 \text{H}_2\text{O}$ . *Inorganic Chemistry*, **33**, 2481–2487.
- Wang A., Freeman J.J., Jolliff B.L. and Chou I.-M. (2006) Sulfates on Mars: A systematic Raman spectroscopic study of hydration states of magnesium sulfates. *Geochimica et Cosmochimica Acta*, **70**, 6118–6135.
- Wildner M. and Giester G. (1991) The crystal structures of kieserite-type compounds. I. Crystal structures of  $\text{Me(II)SO}_4 \cdot \text{H}_2\text{O}$  (Me = Mn, Fe, Co, Ni, Zn). *Neues Jahrbuch für Mineralogie Monatshefte*, **7**, 296–306.
- Witzke T., Wegner R., Doering T., Pöllmann H. and Schuckmann W. (2000) Serrabrancaite,  $\text{MnPO}_4 \cdot \text{H}_2\text{O}$ , a new mineral from the Alto Serra Branca pegmatite, Pedra Lavrada, Paraíba, Brazil. *American Mineralogist*, **85**, 847–849.
- Zaragoza Vérez, G., Rodríguez Vázquez, C.J., Fernández Cereijo, I., González del Tánago, J., Jiménez Martínez, R., Dacuña Mariño, B., Barreiro Pérez, R., Vázquez Fernández, E., Gómez Dopazo, M. and Lantes-Suárez, O. (2022) Ermeloite, IMA 2021-017a. CNMNC Newsletter 68. *Mineralogical Magazine*, **86**, <https://doi.org/10.1180/mgm.2022.93>